THE MAGNETIC HELICITY BUDGET OF A CME-PROLIFIC ACTIVE REGION

L. M. GREEN[1], M. C. LÓPEZ FUENTES[2,*], C. H. MANDRINI[2,**], P. DÉMOULIN[3], L. VAN DRIEL-GESZTELYI[1,3,4,5] and J. L. CULHANE[1]

[1]*Mullard Space Science Laboratory, Univ. College London, U.K. (e-mail: lmg@mssl.ucl.ac.uk)*
[2]*Instituto de Astronomía y Física del Espacio, IAFE, CC. 67 Suc. 28, 1428 Buenos Aires, Argentina (e-mail: lopezf@iafe.uba.ar,mandrini@iafe.uba.ar)*
[3]*Observatoire de Paris, section Meudon, LESIA (CNRS), F-92195 Meudon Principal Cedex, France*
[4]*Centre for Plasma Astrophysics, K.U. Leuven, Celestijnenlaan 200B, 3001 Heverlee, Belgium*
[5]*Konkoly Observatory, Hungary*

(Received 7 November 2001; accepted 12 March 2002)

Abstract. Coronal mass ejections (CMEs) are thought to be the way by which the solar corona expels accumulated magnetic helicity which is injected into the corona via several methods. DeVore (2000) suggests that a significant quantity is injected by the action of differential rotation, however Démoulin *et al.* (2002b), based on the study of a simple bipolar active region, show that this may not be the case. This paper studies the magnetic helicity evolution in an active region (NOAA 8100) in which the main photospheric polarities rotate around each other during five Carrington rotations. As a result of this changing orientation of the bipole, the helicity injection by differential rotation is not a monotonic function of time. Instead, it experiences a maximum and even a change of sign. In this particular active region, both differential rotation and localized shearing motions are actually depleting the coronal helicity instead of building it. During this period of five solar rotations, a high number of CMEs (35 observed, 65 estimated) erupted from the active region and the helicity carried away has been calculated, assuming that each can be modeled by a twisted flux rope. It is found that the helicity injected by differential rotation ($\approx -7 \times 10^{42}$ Mx^2) into the active region cannot provide the amount of helicity ejected via CMEs, which is a factor 5 to 46 larger and of the opposite sign. Instead, it is proposed that the ejected helicity is provided by the twist in the sub-photospheric part of the magnetic flux tube forming the active region.

1. Introduction

Observations of helical magnetic structures in the photosphere, corona and solar wind have attracted considerable attention, with the consequent interest in magnetic helicity studies (see reviews in Brown, Canfield, and Pevtsov, 1999), in many areas of solar activity. Magnetic helicity plays a key role in magnetohydrodynamics (MHD) because it is one of the few global quantities which are preserved. Helicity is conserved in ideal MHD, but it can also be considered a conserved quantity in resistive MHD on time scales shorter than the global diffusion time

*Fellow of CONICET, Argentina.
**Member of the Carrera del Investigador Científico, CONICET, Argentina.

Solar Physics **208:** 43–68, 2002.

scale (Berger, 1984). The energy which may be used to power flares and coronal mass ejections (CMEs) is thought to come from the magnetic field in active regions (ARs). Conversely to magnetic energy, which is efficiently transported to the small spatial scales, magnetic helicity cascades to the large scales. Then, magnetic energy is much more rapidly dissipated (transformed into other forms of energy) than magnetic helicity. The conservation of magnetic helicity gives an important tool for understanding the link between phenomena present in very different physical conditions, such as in the convective zone, the corona and the interplanetary medium.

Low (1996) discussed the dissipation of magnetic helicity under conditions of large magnetic Reynolds number in the solar corona. In this situation resistive effects occur in spatially very localized regions and reconnection drives the redistribution of magnetic helicity within the coronal volume. Since helicity is well preserved, it will accumulate in the corona indefinitely unless it is removed by some means. Rust (1994) and Low (1996) suggested that CMEs are the natural way through which the corona is able to expel the accumulated helicity. Observationally, CMEs have been linked with the ejection of helical structures from the corona (see, e.g., Cliver and Hudson, 2001). Computations carried out by DeVore (2000) indicated that differential rotation can account for the amount of helicity ejected via CMEs. However, Démoulin *et al.* (2002b) analyzed observations of a long-lived, isolated bipolar active region and found that the helicity generated by differential rotation was too small, by a factor of at least 2.5 to account for the coronal helicity and by a factor of at least 5 to account for helicity lost via CMEs. However, they found the same amount of helicity injected via differential rotation as DeVore (2000); the difference between these two works is in the number of CMEs associated with an AR by each study. In the paper by Démoulin *et al.* (2001b) the CME number is the observed one (26 CMEs), while DeVore (2000) uses a mean CME number per AR (5 CMEs) based on SMM observations.

In this paper, we extend the work of Démoulin *et al.* (2002b) by determining the helicity budget of NOAA AR 8100 during five solar rotations. The AR is located in the southern hemisphere and has a negative helicity when it emerges, opposite to the usual hemispheric helicity for the southern hemisphere (Pevtsov, Canfield, and Metcalf, 1995). This AR was very prolific in producing CMEs, and we have estimated that a total of 65 CMEs originated from it during the five solar rotations. The orientation of the main polarities in AR 8100 is initially consistent with the Hale-Nicholson polarity law for solar cycle 23 (leading polarity negative, following positive; Hale and Nicholson, 1925). However, the main photospheric flux concentrations rotate one around the other by approximately 150 deg during the analyzed five solar rotations. This has been considered as indicative of the emergence of a distorted flux tube (López Fuentes *et al.*, 2001) that may probably be a remnant from the previous cycle, so that the true leading polarity should, in fact, be the positive one.

The paper begins with the description of the data used in the study (Section 2.1). The long-term evolution of the photospheric magnetic field is summarized in Section 2.2; while in Section 2.3, Section 2.4 and Section 2.5 we describe the evolution of the coronal emission and the CME activity. The computation of the coronal magnetic field is presented in Section 2.6 and its evolution in Section 2.7. In Section 3 we discuss the method used to compute the helicity injected into AR 8100 by differential rotation and the results found. Computations for the coronal magnetic helicity are discussed in Section 4. In Section 5 we calculate the helicity lost from the coronal fields on the assumption that CMEs are the process by which the solar corona removes magnetic helicity. Comparisons between the amount of helicity generated by differential rotation, the values computed in the corona and the amount lost via CMEs are made in Section 6. There, we also discuss our results and conclude.

2. The Long-Term Evolution of AR 8100

2.1. THE DATA

At the time of our study there were other ARs on the solar disk that, besides AR 8100, may contribute to the CME budget. The identification of all CMEs launched from AR 8100 was made using spacecraft data together with ground based data to find clues at different atmospheric levels about the source region of CMEs. The data set consists of images obtained with instruments on board the SOHO and *Yohkoh* spacecraft, together with Hα data from Hiraiso Observatory (Japan) and Kanzelhöhe Observatory (Austria) for information about filament evolution.

The Large Angle and Spectroscopic Coronagraph (SOHO/LASCO) images the solar corona from 1.1–30 solar radii (Brueckner *et al.*, 1995). Two coronagraphs have been used in this study to identify white-light CMEs; the LASCO C2 (2–6 solar radii) and C3 (4–30 solar radii). Changes in the lower corona, associated to the source region of the CMEs, were identified in data from the Extreme-Ultraviolet Imaging Telescope (SOHO/EIT, Delaboudinière *et al.*, 1995) which images the chromospheric and coronal material through four filters. Two filters were used in particular. The 195 Å band ($T \approx 1.5 \times 10^6$ K) in which a CME watch is run with an image cadence of approximately 12 minutes, providing a good coverage of events in the lower corona. Also, the 304 Å band filter was used ($T \approx 8.0 \times 10^4$ K) in which filament eruptions are well observed. Full disc and partial frame data were obtained from the Soft X-ray Telescope (*Yohkoh*/SXT, Tsuneta *et al.*, 1991) using in particular the Dagwood (AlMg) and Al12 filters. The photospheric magnetic field evolution and computations of the coronal magnetic field were made using data from the Michelson Doppler Imager (SOHO/MDI, Scherrer *et al.*, 1995), which measures the line-of-sight magnetic field at the photosphere. Full-disk 5-min averaged magnetogram data were selected.

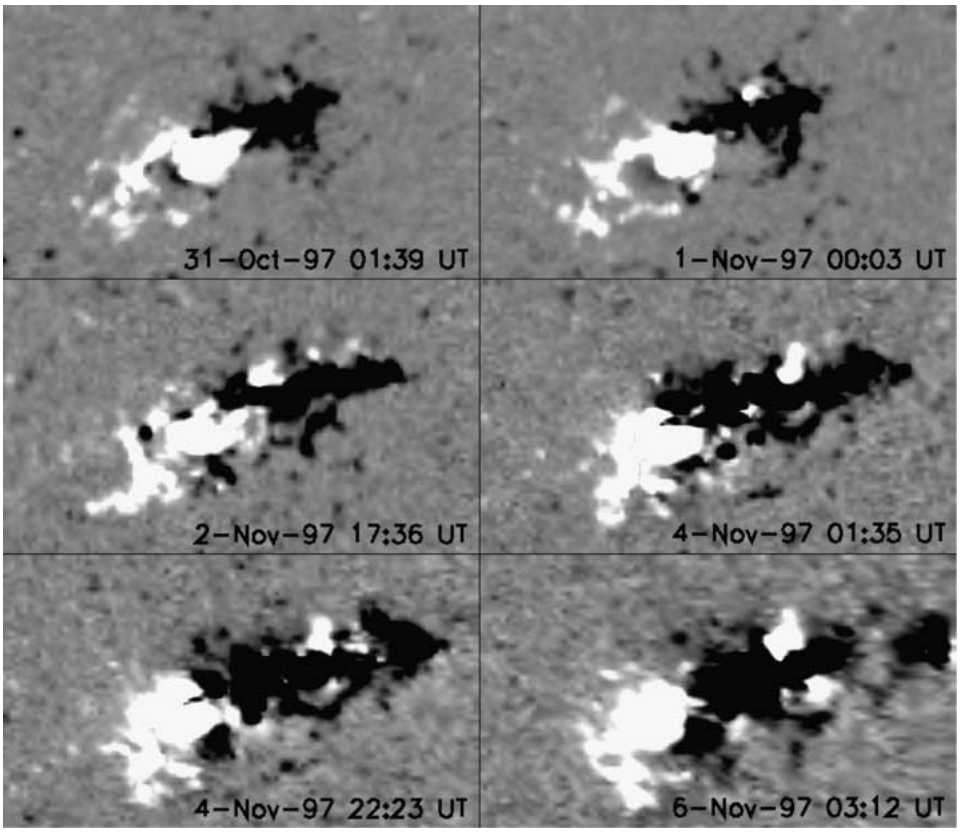

Figure 1. Evolution of the longitudinal magnetic field as observed with SOHO/MDI during the first rotation of AR 8100 (*white*: positive polarity, *black*: negative polarity). Several small bipoles emerge during the AR disc transit that crosses the central meridian (CM) on 2 November, 1997. Notice that until early 4 November, the preceding polarity seems to extend over the following one; while as the AR approaches the west limb (e.g., images on 4 November) it retracts and starts stretching below it (see Section 2.7 for a discussion). The size of the boxes is 310 × 178 Mm, the spatial coordinates have been corrected from projection effects. North is up and west is to the right.

2.2. Evolution of the photospheric magnetic field

AR 8100 was born on the Sun on 28 October 1997 at S21, E67 with a β-type configuration. The AR had a negative leading polarity as is expected from the Hale–Nicholson law for solar cycle 23. The AR emerged into a region of dominantly negative polarity. The passage of the AR could be followed across the disc until it disappeared over the west limb on 9 November 1997. Along this time it evolved to become a δ configuration. A high level of flaring and CME activity was observed (see Section 2.4). During the first rotation, MDI data showed the emergence of secondary new bipoles starting on 1 November 1997 (Figure 1). The emergence continued until 3 November 1997. This new flux emergence led to the formation of new sunspots and to a δ classification. This AR presented the unusual feature

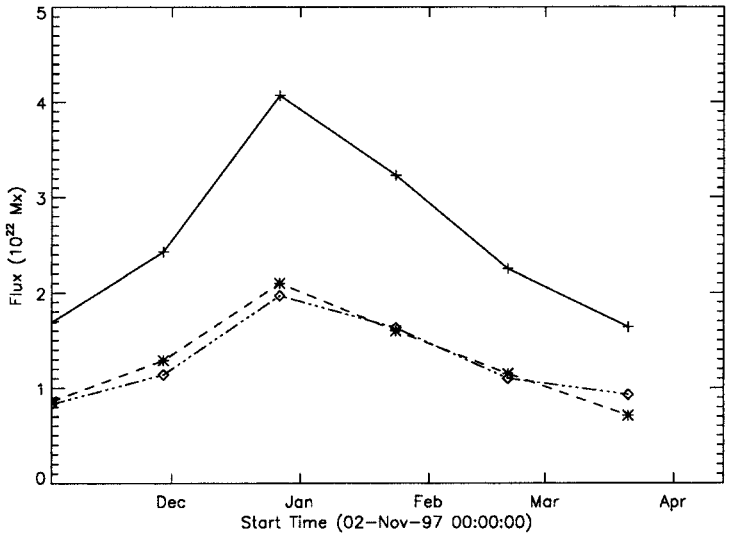

Figure 2. Evolution of the total unsigned (*continuous line*), positive (*dashed line*), and negative (*dashed-dot line*) photospheric magnetic flux in AR 8100. The longitudinal magnetic field of MDI at central meridian passage has been used.

that the leading negative polarity was dispersed and the following positive one was more compact (Figure 1, see also van Driel-Gesztelyi, Schmieder, and Poedts, 2001).

The emergence of flux observed during the first rotation continued even when the AR rotated out of sight; furthermore, there was an increase in flux until the third rotation (Figure 2). A new bipole emerged into the decaying AR around the central meridian passage (CMP) during the third rotation; this bipole was highly inclined, almost perpendicular to the solar equator (see magnetogram on 27 December in Figure 3).

Figures 1 and 3 show MDI magnetic maps for AR 8100 at or close to CMPs (CMP occurs on 2 November in the first rotation, and on 23 January in the fourth rotation) for 5 solar rotations. The data reveal a clockwise rotation of the polarities from the initial configuration, in which the preceding spot is closer to the equator following Joy's law (Hale *et al.*, 1919; Zirin, 1988), through more than 150 deg. López Fuentes *et al.* (2001) have interpreted this kind of motion as being due to the emergence of a deformed flux tube. The evolution of the flux distribution at the photospheric level was dominated by this rotation, but flux emergence, magnetic field cancellation and differential rotation also played a part. We will refer to the AR as 8100 over all the rotations, although in rotation two it is called AR 8112, in rotation three there is new flux emergence and the region appears as AR 8124, in rotation four as AR 8142, while no number is assigned to the region in rotation five.

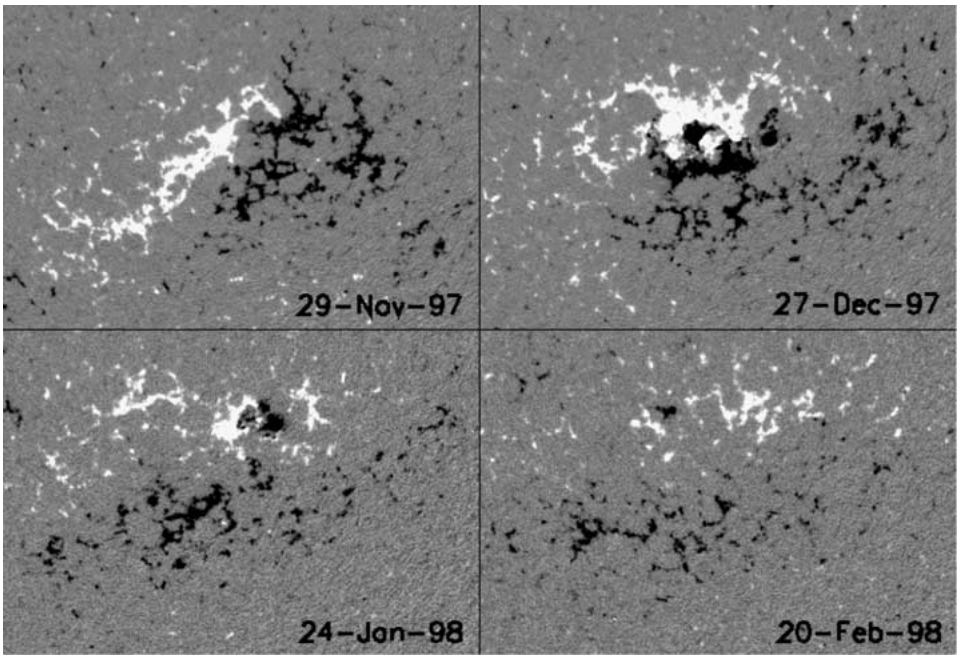

Figure 3. SOHO/MDI magnetic maps showing the long-term evolution of AR 8100 from the second to the fifth rotation. The sizes of the boxes are 538 × 366 Mm. The convention for the figure is the same as in Figure 1.

2.3. Evolution of the coronal loops

The coronal soft X-ray emission evolved as new flux emerged into the AR, old flux decayed and the overall orientation of the polarities changed (see Figure 5). During the first solar rotation, the soft X-ray emission was high and covered a fairly compact region. By the third rotation a new bipole emerged in the central part of the AR, this produced an enhanced soft X-ray emission which remained until the fourth rotation. As the AR decayed the soft X-ray emission became more diffuse and covered a larger area reflecting the flux dispersion. On a larger scale length, the AR was connected to another one (AR 8102) located in the northern hemisphere during the first rotation. This was especially well seen on 3 November 1997. The connection to this AR was highlighted by a dimming event observed in EIT data produced during a CME which partially opened the trans-equatorial inter-connecting structure (Delannée and Aulanier, 1999).

2.4. The activity in AR 8100

AR 8100 has been well studied during its first rotation as it showed a high level of CME and flare activity (Green *et al.*, 2001). Several flare-associated CMEs were observed, including events on 3 November 1997 at 10:31 UT (Delannée and Aulanier, 1999) and an X9.4 class flare on 6 November 1997 (Maia *et al.*,

TABLE I

The CMEs ejected by AR 8100. The first and second columns indicate the date and time of the first appearance in LASCO C2. The third column gives the maximum angular extension in degrees of the CME (projected in the plane of sky), the values were taken from the catalog prepared by C. St. Cyr (GFSC) . The fourth column indicates with H the halo CMEs and with T the large-scale trans-equatorial events. In the last column we show the position of the AR at the time of the CME; rotation phase 0.00 means that the AR is at CMP on the first rotation, 0.25 that it is at the west limb, and so on. Rotation phase numbers increase as the AR repeatedly crosses the central meridian.

Date	Time (UT)	CME span	H/T	Rotation phase
2 Nov. 1997	11:44	70		0.00
2 Nov. 1997		no white light		0.00
3 Nov. 1997	05:28	90		0.04
3 Nov. 1997		within previous event		0.04
3 Nov. 1997	11:11	195	T	0.04
4 Nov. 1997	06:10		H	0.07
5 Nov. 1997	00:18	98		0.11
5 Nov. 1997	07:29	within previous event		0.11
5 Nov. 1997	12:10	narrow		0.11
5 Nov. 1997	17:53	no white light		0.11
6 Nov. 1997	00:44	18		0.14
6 Nov. 1997	04:20	57		0.14
6 Nov. 1997	12:10	261		0.14
7 Nov. 1997	00:43	29		0.18
8 Nov. 1997	08:59	74		0.21
28 Nov. 1997	13:55	74		0.96
27 Dec. 1997	01:01	33	T	2.00
30 Dec. 1997	05:10	70		2.11
1 Jan. 1998	15:19	16		2.18
17 Jan. 1998	12:00	37		2.75
19 Jan. 1998	06:06	59		2.82
21 Jan. 1998	17:27	168		2.89
26 Jan. 1998	23:57	54		3.07
28 Jan. 1998	03:27	23		3.14
28 Jan. 1998	14:56	62		3.14
30 Jan. 1998	14:31	21		3.21
1 Feb. 1998	22:37	18		3.29
14 Feb. 1998	00:00	52		3.75
15 Feb. 1998	17:27	35		3.82
17 Feb. 1998	05:08	59		3.89
18 Feb. 1998	02:27	28		3.93
21 Feb. 1998	04:26	31		4.04
26 Feb. 1998	05:27	55		4.21
27 Feb. 1998	09:55	53		4.25
17 Mar. 1998	12:34	202		4.93

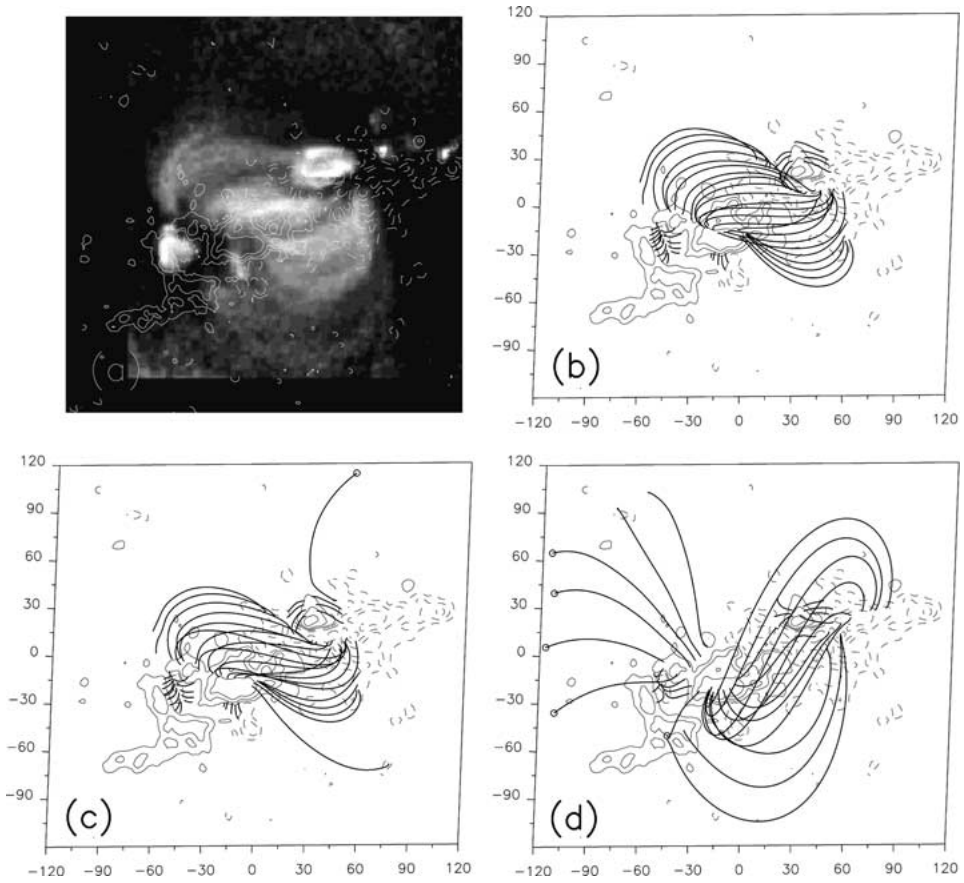

Figure 4. *Yohkoh*/SXT observation and linear force-free computations of the coronal field using SOHO/MDI magnetograms from the first rotation of AR 8100. (a) *Yohkoh*/SXT observation. (b) Linear force-free field computation with $\alpha = -1.26 \times 10^{-2}$ Mm^{-1}. This value produces the best fit to the observed coronal field and is used to compute the coronal helicity as discussed in Section 4. (c) Linear force-free field computation with $\alpha = -1.51 \times 10^{-2}$ Mm^{-1} gives an extrapolation of field lines that do not match well the SXT loops. (d) represents a computation using $\alpha = +1.26 \times 10^{-2}$ Mm^{-1} and shows that the SXT loops are not well fitted by a positive α. The abscissas and ordinates in each map are expressed in Mm. ISO-contours ($\pm$ 50, 200, 500 G) of the line-of-sight magnetic field have been drawn with *continuous/dashed lines* for positive/negative values.

1999). Yan *et al.* (2001) modeled the AR 3-D magnetic field around the time of an X2 flare on 4 November 1997. These computations reveal the presence of high magnetic shear in the AR. Flare and CME activity were at their highest level during the first rotation. Significant data gaps, both in LASCO and EIT, occurred during the second rotation, but several CMEs were observed in the third, fourth and fifth rotations. Table I lists the characteristics of the CMEs observed during the life of

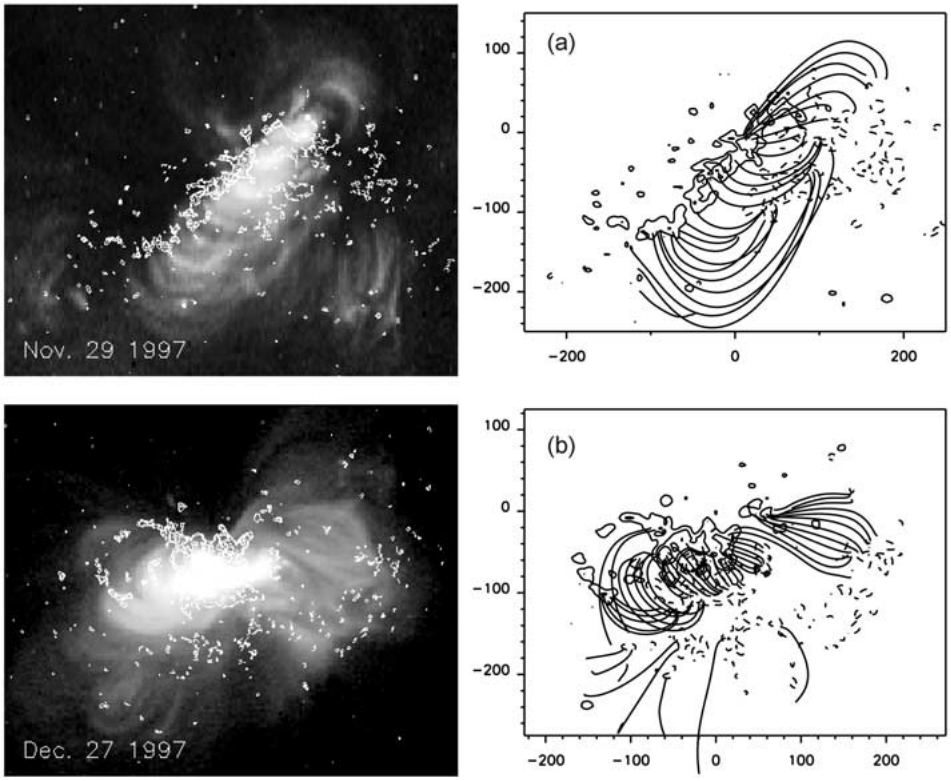

Figure 5a,b

Figure 5. Yohkoh/SXT observations and linear force-free computations of the coronal field using SOHO/MDI magnetograms from the second (a) to the fifth (d) rotation of AR 8100. The α value is selected to have the best global match between the SXT loops and the computed field lines (see Sections 2.6, 2.7, and Table I). The abscissas and ordinates in each map are expressed in Mm. ISO-contours ($\pm$ 50, 200, 500 G) of the line-of-sight magnetic field have been drawn with *continuous/dashed lines* for positive/negative values.

AR 8100. The angular size of a CME (or CME span), as viewed with LASCO, gives an indication of the CME spatial size but this is biased by projection effects.

The third column in Table II shows the number and GOES X-ray class for the flares occurring in AR 8100, while the observed and corrected CME numbers (see below) are listed in the fourth and fifth columns. The number of flares was determined by combining GOES observations and ground based data from the Hα daily reports on *Solar Geophysical Data* (*SGD*). Accumulated data gaps of about one to two days long per solar rotation were present in SGD reports. The number and intensity of the flares decreased remarkably from the first to the second rotation, while during the third rotation they became high again. The emergence of new flux at the central portion of the AR (Figure 3) is the most likely origin of this increase. Flare activity decreased by the fourth and disappeared by the fifth

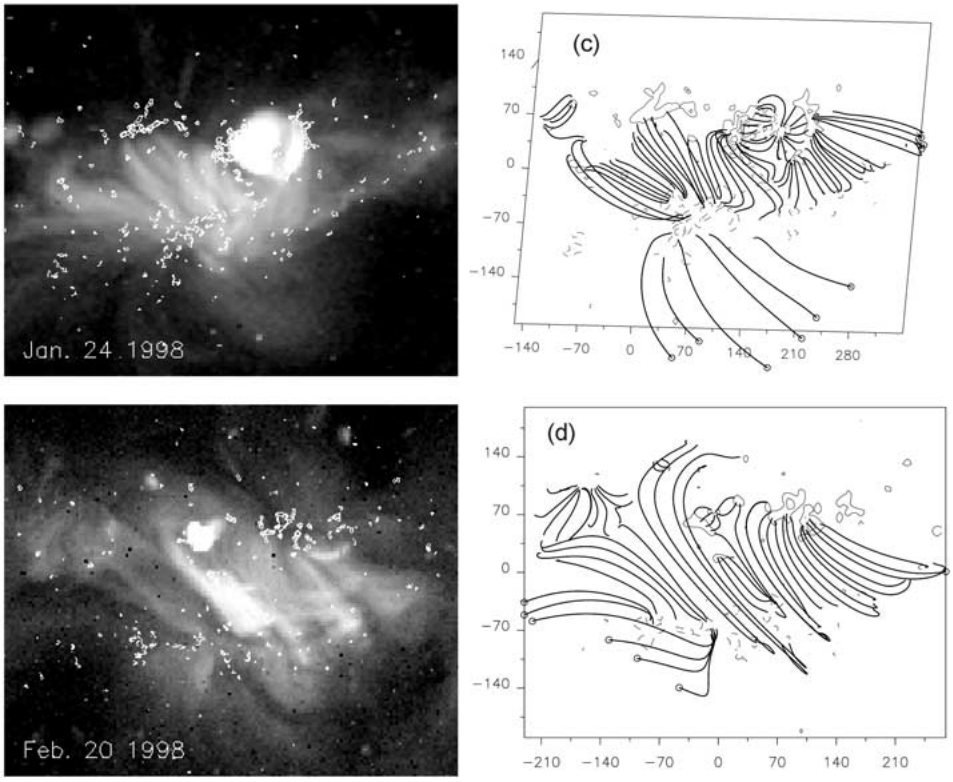

Figure 5c,d.

rotation. CME production was high throughout the AR evolution. This indicates that, even if flares and CMEs share some common physical mechanisms (like the instability of the magnetic field and magnetic reconnection), they are distinct phenomena. The flare importance and the number of flares depend more on the free energy locally available (e.g., formation of strong current layers), while the CME production depends more on global quantities, in particular the amount of magnetic helicity (Low, 1997).

2.5. THE CMES LAUNCHED BY AR 8100

The identification of the AR, which may be the source of a given CME, is not an easy task as there are many other features on the disk that can be its origin. LASCO C2 and C3 data were carefully analyzed to check for the existence of white light CMEs and to compute their span (Table I). To determine the number of CMEs ejected by AR 8100, we have taken into account lower coronal signatures. These include post-eruption arcade formation and cusp features in SXT, waves (Thompson *et al.*, 1999), and dimmings in EIT (which indicate a reduction in the density of the coronal plasma, see Sterling and Hudson, 1997; Zarro *et al.*,

1999). Filament disappearances were also looked for in Hα data. Endeavoring to include all the CMEs coming from AR 8100, we have also considered ejections that have the correct span to encompass the AR but for which no signature can be seen anywhere on the disc. In these instances it is possible that the lower coronal signatures have been missed because of the cadence of the data. Thus, the total number of CMEs observed coming from AR 8100 when on the visible side of the Sun amounts to 35 (Table II).

The real number of CMEs ejected by AR 8100 is, of course, larger than the observed one, which has to be corrected because of two different kinds of gaps in the observations. The first one comes from the lack of continuity in LASCO and EIT observing times, while the second one is due to the passage of the AR behind the visible side of the Sun. Accounting for CMEs, which occurred during the times when LASCO and EIT were not observing for at least three hours, can be done by computing an average number of CMEs per day from the days without gaps, and assuming that the CME frequency is the same during the gaps. This correction turned out to be a minor one since the CME count was increased in only 0.6 events. The only noteworthy gap (3 days in a row) occurred during the second rotation, when we have no observed CME. The number of CMEs which could originate from the AR when it was located on the far side of the Sun has been estimated in a subjective way, supposing a continuity in CME productivity. Given a certain rotation, we averaged the number of CMEs from the preceding and following AR disc passages and we assigned this number to the period when the AR was on the invisible side of the Sun. In the case of the first rotation only half of the AR disc passage (from 2 November to 8 November) was considered for the preceding rotation (the AR was born on the disc on 28 October 1997). After correcting for both kinds of gaps, we find that AR 8100 appears to be the source of 65 CMEs.

2.6. Determination of the coronal magnetic field

The coronal field is computed under the linear (or constant α) force-free field assumption:

$$\nabla \times \mathbf{B} = \alpha \mathbf{B}, \tag{1}$$

using a fast Fourier transform method as proposed by Alissandrakis (1981). The value of α in Equation (1) is determined through an iterative process. First, we compute the coronal field assuming a given value for α; then, we compute the mean distance between the observed SXT coronal loops and the closest computed field lines. Finally, through successive steps we select the value of α that gives the best global fit (i.e., lowest mean distance). More precisely, we first define a series of points along the central axis of each observed loop. Then, we compute the best fitted field line to each loop in three steps as follows:

(1) In the first step, field lines in the surroundings of a given loop are kept for the next step only if their end points are closer than a given distance $d_{\min}$ to the

TABLE II

The columns of the table give, respectively: the rotation number, the starting rotation date (CMP of AR 8100), the number of flares for each GOES X-ray class (taken from the catalog at *http://www.lmsal.com/SXT* correlated with *Solar Geophysical Data* reports on Hα flares), the number of observed CMEs, the corrected CME numbers and the value of the α parameter. The corrected CME numbers were obtained assuming that the frequency of the CMEs during data gaps in LASCO and EIT observations, and periods when the AR was on the far side of the Sun, is the same as during observing times (see Section 2.5).

Rot.	Date	Flares (GOES)				CMEs	CMEs	α
		X	M	C	B	obs.	corr.	$10^{-2}\mathrm{Mm}^{-1}$
1	2 Nov. 1997	2	4	24	5	16	24.1	−1.26
2	29 Nov. 1997	–	–	3	4	–	2.5	0.94
3	27 Dec. 1997	–	1	7	8	6	11.7	0.82
4	23 Jan. 1998	–	–	3	3	9	16.8	0.94
5	20 Feb. 1998	–	–	–	–	4	9.6	1.00
Total		2	5	37	20	35	64.7	

loop ends ($d_{\min}$ is an upper limit for the length of the unobserved part of the feet of the loop).

(2) In the second step, we compute iteratively the mean distance, d_{mean}, between the loop and each field line because we cannot associate a loop position to a field line point. For a given loop point, we compute the closest distance to the selected field line. Then, the mean distance is defined by the average of the individual distances computed for all the loop points. We then keep the field line which has the closest mean distance to the loop.

(3) In the third step, we test if in the surroundings of the field lines, which have been kept, there are other lines which are even closer to the loop. This is achieved by computing a new set of field lines, closely spaced, and restarting the procedure from the first step. The iterative procedure is stopped when no significant decrease in the mean distance d_{mean} can be obtained.

The above procedure gives a mean distance for each loop and each α value. The minimization of this distance gives a quantitative way to determine the best α value for each loop. The spread in the best α values for the set of loops gives an estimation of the error in α, and the minimization of the mean distance averaged over the loops, $\langle d_{\mathrm{mean}} \rangle$, determines which α value best fits globally the observations.

For the present study we use $d_{\min} = 20$ Mm, a reasonable upper limit for the length of the unobserved part of the loop from its X-ray end to the photosphere. For example, the results for the first rotation (see Figure 4) are: $\alpha_{\mathrm{closest}} \approx -1.26 \times 10^{-2}\ \mathrm{Mm}^{-1}$, which minimizes $\langle d_{\mathrm{mean}} \rangle$ to a value of 1.6 Mm. This value of $\langle d_{\mathrm{mean}} \rangle$ is very close to the pixel resolution of SXT ($\approx$ 1.8 Mm). On both sides of

α_{closest}, $\langle d_{\text{mean}} \rangle$ increases to 2.0 Mm for $\alpha \approx -1.51 \times 10^{-2}$ and -0.75×10^{-2} Mm^{-1}. For a potential field $\langle d_{\text{mean}} \rangle \approx 4$ Mm. Using a positive α value ($\alpha = 1.26 \times 10^{-2}$ Mm^{-1}) we find $\langle d_{\text{mean}} \rangle \approx 6.5$ Mm. However, there are two loops that cannot be fitted at all with the above d_{min} value and a positive α! This shows that a potential field or a field with positive helicity cannot explain the observed SXT loops. For individual loops, the minimum mean distance is found for a range of α which is asymmetric with respect to the above mean value, $[-1.6 \times 10^{-2}, -0.6 \times 10^{-2}]$ Mm^{-1}. The mean deviation to α_{closest} is found to be 0.32×10^{-2} so 25% of α_{closest}. For all loops the minimum value of d_{mean} is of the order, or slightly below, the SXT pixel size. The range of α found reflects mostly the non-uniformity of α in the AR and gives an idea of the limitations of a constant α field approach.

As an example of the quality of our magnetic field model, Figure 4 shows the best mean fit (panel b) to the SXT loops (panel (a)) in the first rotation. Note that a negative α corresponds to an inverse S-shape. Panel (c) in Figure 4 shows a model with $\alpha = -1.51 \times 10^{-2}$ Mm^{-1}, which is an increase of 20% with respect to α_{closest}. To compare how the variation in α affects the modeled field lines, we show field lines which start from the same location. It is clearly seen that for a change of 20% in α the modeled field lines, although they globally follow the trend, do not match the SXT loops as well as the α_{closest} model does.

2.7. Evolution of the Computed Coronal Magnetic Field

Table II (last column) lists the values of α for the five rotations we have analyzed. During the first rotation α takes a negative value, which means that AR 8100 does not follow the hemispheric chirality-rule since a positive twist is dominant in the southern hemisphere (Seehafer, 1990; Pevtsov, Canfield, and Metcalf, 1995). Figure 4(d) shows that a positive α is not suited to match the observed loops, which globally show an inverse S-shape implying a negative value of α (Pevtsov, Canfield, and Metcalf, 1995; Rust and Kumar, 1996; Canfield, Hudson, and McKenzie, 1999).

The presence of twist in an emerging flux tube may influence the distribution of the line-of-sight magnetic field in such a way that, for a negative twist, the preceding polarity extends along the northern boundary of the following polarity (forming an elongated 'tongue'). This has been proposed in López Fuentes *et al.* (2000) (see their Figure 5). If the twist is positive, the distribution of the line-of-sight flux should be a mirror image of the negative one. The overlap of the two elongated portions (or 'tongues') of the main polarities as seen in the first panel of Figure 1 shows that the negative leading polarity extends down the northern boundary of the following polarity and is indicative of the negative twist found. However, as the AR evolved during this first rotation (Figure 5) and new bipoles emerged, the orientation of the tongues changed (as seen when comparing the magnetic map on 31 October to the one on 6 November). This new orientation would imply that the sign of α changes.

We have computed the value of α, as explained above, from 2 November to 5 November. We have found that it changes from -1.3×10^{-2} Mm^{-1} to -0.63×10^{-2} Mm^{-1}, becoming less negative. We interpret this change as being due to the emergence of a new bipole at the location of AR 8100 which presumably carries positive helicity, that is to say of opposite sign to the primary one. From the second rotation on, the value of α stays positive and almost constant (Table II).

3. Magnetic Helicity Injected by Shearing Footpoint Motions

3.1. GENERALITIES

The magnetic helicity of a field $\mathbf{B}$ within a volume V is defined by

$$H = \int_V \mathbf{A} \cdot \mathbf{B} \, \mathrm{d}V \,, \tag{2}$$

where the vector potential $\mathbf{A}$ satisfies

$$\mathbf{B} = \nabla \times \mathbf{A} \,. \tag{3}$$

However, Equation (2) is physically meaningful only when the magnetic field is fully contained inside V (i.e., at any point of the surface S surrounding V, the normal component $B_n = \mathbf{B} \cdot \hat{n}$ vanishes). This is so because the vector potential is defined through a gauge transformation ($\mathbf{A}' = \mathbf{A} + \nabla\Phi$), then H is gauge-invariant only when $B_n = 0$.

Berger and Field (1984) have shown that for cases where $B_n \neq 0$ one can define a relative magnetic helicity (H_r) by subtracting the helicity of a reference field $\mathbf{B}_0$, having the same distribution of B_n on S:

$$H_r = \int_V \mathbf{A} \cdot \mathbf{B} \, \mathrm{d}V - \int_V \mathbf{A_0} \cdot \mathbf{B_0} \, \mathrm{d}V \,. \tag{4}$$

Berger and Field (1984) and Finn and Antonsen (1985) have shown that H_r is gauge-invariant, and that H_r does not depend on the common extension of $\mathbf{B}$ and $\mathbf{B_0}$ outside V.

Since H_r is well preserved under solar conditions (Berger, 1984), the only way helicity can be modified inside V is because of helicity flux crossing the boundary S. The change of relative helicity is given by (Berger and Field, 1984)

$$\frac{\mathrm{d}H_r}{\mathrm{d}t} = -2 \int_S [(\mathbf{A_0} \cdot \mathbf{v})\mathbf{B} - (\mathbf{A_0} \cdot \mathbf{B})\mathbf{v}] \, \mathrm{d}\mathbf{S}, \tag{5}$$

where $\mathbf{v}$ is the velocity of the plasma. The last term on the right-hand side of Equation (5) represents a transport of magnetic helicity across S. In the case studied

below, where S is at the photospheric level, this term cannot be evaluated as no transverse field measurements are available. Therefore, we will consider only the first term in the right-hand side of Equation (5). This term represents the injection of helicity by plasma motions parallel to the surface S. Computing $\mathbf{A_0}$ as a function of the B_n distribution, Berger (1984, 1988) derived an expression for $\mathrm{d}H_r/\mathrm{d}t$ that depends only on observable photospheric quantities (B_n and $\mathbf{v}$):

$$\frac{\mathrm{d}H_r}{\mathrm{d}t} = -\frac{1}{\pi}\int_S\int_S \frac{\mathbf{R}\times\mathbf{v}(\mathbf{r})}{R^2} B_n(\mathbf{r})B_n(\mathbf{r}')\,\mathrm{d}S\,\mathrm{d}S', \tag{6}$$

where $\mathbf{R} = \mathbf{r} - \mathbf{r}'$ is the difference in spatial positions on the photospheric plane. This equation involves a double integration (on $\mathbf{r}$ and $\mathbf{r}'$) on the magnetogram.

We will apply the previous results to the case where photospheric motions are restricted to differential rotation. We will consider the following classical expression for differential rotation:

$$\omega(L) = a + b\,\sin^2 L + c\,\sin^4 L\,, \tag{7}$$

where L stands for the latitude. Such angular velocity induces a shear flow which transforms the photospheric flux distribution, injecting helicity into the corona. In numerical applications below, we will take $a = 14.38$ deg day^{-1}, $b = -1.95$ deg day^{-1}, $c = 2.17$ deg day^{-1} as given by the cross-correlation analysis of Kitt Peak magnetograms from 1975 to 1991 (Komm, Howard, and Harvey, 1993). Including Equation (7) in Equation (6) we can find the injection of relative helicity by differential rotation (Démoulin *et al.*, 2002a).

3.2. The helicity injected in AR 8100

The magnetic helicity injected into AR 8100 per solar rotation ($\Delta H_{d.r.}$), as computed from Equation (6), is summarized in the fourth column of Table III. Since by the end of the first rotation it is likely that the sign of the magnetic helicity had changed due to new flux emergence carrying positive helicity, accompanied by helicity cancellation and CME activity (see Section 2.7), we have analyzed separately the AR helicity injection from 2 November to 5 November (first line in Table III). We also give a range for the helicity injection, since the flux emergence (Figure 2) observed during the first three rotations changes the distribution of the photospheric field altering the computed values when only the distributions at CMPs are considered.

The helicity injection rate by differential rotation changes sign as AR 8100 evolves and rotates (see Figure 6). It is worth noting that this occurs even when the differential velocity profile remains the same. This change of sign is due to the competition between two effects: the rotation of each polarity (twist helicity) and the relative rotation of positive and negative polarities (writhe helicity). In the case of differential rotation, twist and writhe injection rates always have opposite signs

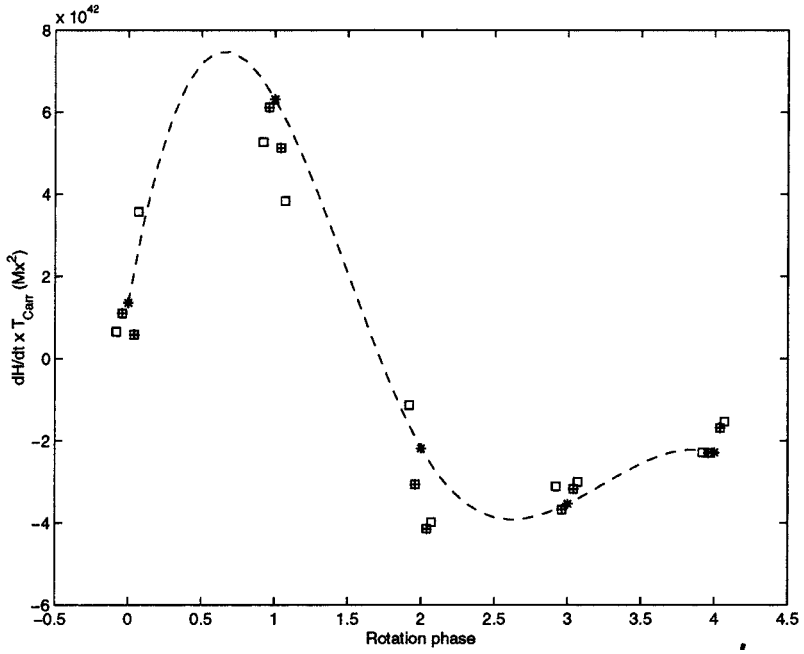

Figure 6. Evolution of the injection rate of magnetic helicity ($\mathrm{d}H_r/\mathrm{d}t\ T_{\mathrm{Carr}}$) by differential rotation versus time for AR 8100 (T_{Carr} is the Carrington rotation period). MDI magnetograms at each CMP (*asterisks*), ± 1 (*squares with a cross*) and ± 2 days (*squares*) from CMP have been used to compute $\mathrm{d}H_r/\mathrm{d}t$. A spline curve computed using only the CMP values has been added. The points are very spread around the CMP values during the first three rotations when flux was still emerging in AR 8100, while they follow closely the curve during the last two rotations (see Section 3.2).

(Démoulin *et al.*, 2002a). It is the orientation of the bipolar magnetic field which mainly determines the amount of helicity injected by writhe. If the axis of the bipole is more aligned with the north-south direction, writhe injection dominates over twist injection; while it is the opposite if the bipole is more aligned in the East-West direction. This gives a well-marked change in the sign of the injection rate (this change can be deduced qualitatively from Figure 6 of Démoulin *et al.*, 2002a). The magnetic polarities in AR 8100 are rotating not only due to the effect of differential rotation, but there is also present a large intrinsic rotation as shown in Figure 3 (see also López Fuentes *et al.*, 2000 for the study of another rotating AR). Considering the full period, from the second to the fifth rotation, the total helicity injected into AR 8100 by differential rotation is $\approx -7.3 \times 10^{42}$ Mx^2.

Another way to inject magnetic helicity into the corona is by localized photospheric shearing motions. In our particular case, shearing motions were evident from magnetogram movies only during the first rotation between the two main polarities of the main AR bipole, and between the new emerging bipoles at the north of the AR and the main negative polarity (Figure 1). We have computed the helicity injected by shearing motions from 2 to 5 November using Equation (11)

in Démoulin *et al.* (2002b). We estimate the angular variation in the position of the moving flux concentrations and their fluxes from MDI magnetograms along these three days. Our aim is to obtain an order of magnitude estimate for this injection, a more detailed analysis as has been done by Chae (2001) and Chae *et al.* (2001) would be required for a precise computation. We obtain a helicity injection of $\approx 8 \times 10^{40}$ Mx^2 when considering the displacement of the new emerging polarity with respect to the main negative one, and of $\approx 5 \times 10^{41}$ Mx^2 for the motion between the two main polarities forming the main bipole. These values are in agreement with the one found by Chae (2001), and one order of magnitude lower than the one in Chae *et al.* (2001). Adding up the two previous values, it can be seen that they are of the same order of magnitude and sign as the helicity injected along the same period of time by differential rotation ($\approx 5 \times 10^{41}$, Table III). We want to emphasize that we have considered the two strongest motions observed at that time, and that no other significant localized shearing motions were seen during the following solar rotations of AR 8100.

4. The Coronal Magnetic Helicity

We have computed the coronal H_r ($H_{\rm cor}$) of AR 8100, as discussed in the Appendix, for the magnetic field models obtained from MDI magnetograms and shown in Figures 4 and 5. The calculation has been made using the linearized expression in α for $H_{\rm cor}$, called $H_{r,\rm lin}$; therefore, the error in our estimated values of the model helicity is 25% since it comes from the mean deviation to $\alpha_{\rm closest}$. We have taken a computational box centered in the AR and having the same extension (500 Mm) in all cases.

Considering the first line in Table III, it can be seen that from 2 to 5 November 1997, the absolute value of the coronal helicity increases significantly. This change cannot be the result of the injection by differential rotation ($\Delta H_{\rm d.r.}$) or shearing motions, which turn out to be two orders of magnitude lower and of opposite sign. Furthermore, as discussed in Section 2.7, the absolute value of α decreases during this period implying that the observed coronal helicity change is mainly due to strong flux emergence.

The coronal helicity, as computed under the linear force-free field assumption, shows a change in sign from negative to positive from the first to the second rotation. This change in sign cannot be explained by the injection of helicity by differential rotation, even though it has the correct sign, because it is an order of magnitude too small to account for the coronal evolution.

From the second rotation onward the coronal helicity is positive and decreases in magnitude. The negative helicity injected by differential rotation can contribute to this decrease, but its magnitude remains too small to explain this decrease until the fourth rotation (compare $\Delta H_{\rm cor}$ to $\Delta H_{\rm d.r.}$ in Table III). We conclude that the he-

licity injected by differential rotation cannot explain the coronal helicity changes, even if we take the minimum of the coronal helicity (given by $H_{r,\mathrm{lin}}$ in Appendix A).

5. The Ejected Magnetic Helicity

A CME is formed by an instability of the coronal field, and so the ejected CME will carry part of the magnetic helicity of its original source magnetic field. There is increasing evidence that this is the case from observations which have shown that the helicity sign of magnetic clouds matches that of their source region. Bothmer and Schwenn (1994), Rust (1994) and Marubashi (1997) have found a high correlation between the helicity sign in magnetic clouds and their associated erupting filaments. Yurchyshyn *et al.* (2001) confirmed these statistical results in two well observed cases. All the CMEs listed in Table I have their origin in AR 8100, and hence, we assume that they are carrying into the interplanetary medium part of the helicity of the AR at the time of their launch. Since we have no way to compute the helicity in a CME, we can only make an association between the number of CMEs ejected by AR 8100 and the magnetic clouds originating from them assuming a one to one correspondence (as done by DeVore, 2000; Démoulin *et al.*, 2002b). It is a strong hypothesis to suppose that each CME detected by LASCO becomes a magnetic cloud but there is increasing evidence that it is likely to be so (Webb *et al.*, 2000). Due to the lack of quantitative data on the magnetic clouds linked to AR 8100, we rather rely on another set of well observed and modeled magnetic clouds.

The magnetic field has been measured in a set of 18 well-observed interplanetary clouds and a close fit to the observations has been obtained using a linear force-free field by Lepping, Burlaga, and Jones (1990). The average value of the axial field in this set of clouds is $B_o = (2.0 \pm 0.7) \times 10^{-4}$ G and their average radius $R = (2.1 \pm 0.7) \times 10^{12}$ cm. Zhao, Hoeksema en Marubashi (2001) have analyzed a set of 23 magnetic clouds (11 are the same ones as in Lepping, Burlaga, and Jones (1990), but their fitting model is different since it takes into account the expansion of the clouds during the spacecraft crossing). Zhao, Hoeksema, and Marubashi found $B_o = (2.4 \pm 0.8) \times 10^{-4}$ G and $R = (1.7 \pm 0.8) \times 10^{12}$ cm values close to those of Lepping, Burlaga, and Jones (1990). Because the magnetic helicity in a cloud depends on the third power of R and second power of B_o (see Equation (17) in Démoulin *et al.*, 2002b), the spread in the measurements has a large effect on our helicity estimation. The mean value for Lepping, Burlaga, and Jones and Zhao, Hoeksema, and Marubashi are respectively $H_{\mathrm{m.cl.}} = 2.4 \times 10^{42}$ and 2.8×10^{42} Mx^2 assuming a cloud length of 0.5 AU. One of the clouds in the set has one order of magnitude larger helicity than the others (it has both a strong B_o and a large R). Excluding this, possibly, peculiar magnetic cloud, the above helicity estimates become $H_{\mathrm{m.cl.}} = 1.9 \times 10^{42}$ and 1.5×10^{42} Mx^2, respectively. Future studies are needed to have more precise values. DeVore (2000) used a helicity per

cloud of 2×10^{42} Mx^2 which is comparable to the above average estimates so we use below this last value (this also permits a direct comparison of our results with DeVore, 2000).

Considering the period from the second to the fifth rotations, since during the first rotation we cannot ascertain which is the sign of the helicity being shed by CMEs (the helicity of the AR changes sign), AR 8100 ejected at least 19 CMEs (Table II). Multiplying that number of CMEs by the above estimate, we find that a magnetic helicity $\approx 38 \times 10^{42}$ Mx^2 was ejected from AR 8100 while differential rotation injected a total negative helicity of $\approx -7.3 \times 10^{42}$ Mx^2 (see Table III). Therefore, the magnetic helicity ejected is a factor ~ 5 larger and of different sign (since at that time the AR helicity is positive and we assume the CMEs to remove positive helicity) than the helicity injected by differential rotation.

Let us now analyze the helicity ejected from 2 to 5 November 1997. The highest CME activity occurs during this time, when 10 CMEs are observed during these three days. During this period the AR helicity is negative; therefore, we assume that the helicity carried away by CMEs is also negative. However, Leamon, Canfield, and Pevtsov (2002), using *in-situ* measurements and assuming that the magnetic cloud axis is parallel to the ecliptic plane, infer a positive helicity sign for the cloud associated to the CME on 4 November 1997; even though the coronal SXT loops at the time of the CME still show and inverse 'S' shape (indicative of a negative helicity, which is opposite to the sign reported by Leamon, Canfield, and Pevtsov). This apparent contradiction may be the result of the change in sign of helicity occurring during the period 4 to 6 November, when the AR may contain magnetic structures with different helicity sign. Despite this, we will still rely below on the statistical results which indicate that the helicity sign is strongly correlated to that of the source region (see references at the beginning of this section). Then, comparing $\Delta H_{\mathrm{d.r.}}$ and $\Delta H_{\mathrm{m.cl.}}$ in Table III, we see that the helicity injected by differential rotation is two orders of magnitude lower than the ejected value, and again of different sign.

The magnetic helicity ejected is subject to several uncertainties. First, because not all CMEs associated with AR 8100 were observed. Second, we have assumed that the average CME helicity corresponds to the average helicity of a magnetic cloud set, with large uncertainties as discussed above, and also probably systematic biases. Third, the length of a magnetic cloud is probably much larger than 0.5 AU for clouds observed at 1 AU distance from the Sun. Bidirectional flows observed in interplanetary clouds indicate that they are probably still rooted in the Sun when observed at 1 AU (e.g., Richardson, Farrugia, and Burlaga, 1991; Richardson, 1997; Shodhan *et al.*, 2000). This implies that the length of clouds should be at least 2 AU, a factor 4 larger than assumed above. Currently, we do not know the distribution of twist along the flux rope of the magnetic cloud (e.g., if the twist is more concentrated in the front or the legs of the magnetic cloud). The simplest hypothesis is to assume that the model of Lepping, Burlaga, and Jones (1990) can be applied to the full extent of the flux rope. Therefore, considering

TABLE III

The budget of the relative helicity is listed per rotation. The total budget on the last line is the sum from the second to the fifth rotation. We have analyzed separately the budget from 2 November to 5 November 1997, because of the change of sign in α during the first rotation (Section 2.7). The coronal helicity ($H_{\rm cor}$) and its change ($\Delta H_{\rm cor}$) are computed from the successive CMP magnetograms. Furthermore, a range is given for the helicity injected by the differential rotation ($\Delta H_{\rm d.r.}$), since flux emergence during the first three rotations (Figure 1) changes the photospheric field altering the values computed when only the CMP distribution is considered. An interval is given for the cloud estimations ($\Delta H_{\rm m.cl.}$) taking the observed and corrected number of CMEs (considering the two limits, 0.5 and 2 AU, for the length of the flux tube in magnetic clouds). All values are in units of 10^{42} Mx^2.

Date Rot.	$H_{\rm cor.}$	$\Delta H_{\rm cor.}$	$\Delta H_{\rm d.r.}$	$\Delta H_{\rm cor.} - \langle \Delta H_{\rm d.r.} \rangle$	$\Delta H_{\rm m.cl.}$ (CME obs.)	$\Delta H_{\rm m.cl.}$ (CME cor.)
2–5 Nov.	–	−33.6	[0.2, 0.8]	−33.1	[−20, −80]	[−20, −80]
2 Nov.	−11.0					
1		33.5	[1.4, 5.1]	30.2	–	–
29 Nov.	22.5					
2		−2.9	[5.1, −4.6]	−3.2	[0,0]	[5, 20]
27 Dec.	19.6					
3		−11.2	[−4.6, −2.8]	−7.5	[12, 48]	[24, 96]
23 Jan.	8.4					
4		−3.3	[−2.8, −1.6]	−1.1	[18, 72]	[34, 136]
20 Feb.	5.1					
5		−2.0	−1.6	−0.4	[8, 32]	[19, 76]
Total 2–5		−19.4	−7.3	−12.2	[38, 152]	[82, 328]

that the magnetic clouds are still rooted in the Sun, we can estimate that during the second to the fifth rotation the total ejected helicity is larger by a factor of 4. If we now consider the corrected CME number, we find that AR 8100 expels during the same period of time $\approx 82 \times 10^{42}$ Mx^2 assuming a flux rope length of 0.5 AU, a factor 11 larger than that which differential rotation provides. Again, if we assume all these magnetic clouds to have a length of 2 AU, the ejected helicity increases by a factor of 4.

6. Discussion and Conclusions

The main question addressed in the present study is whether magnetic helicity is injected into the corona mainly by horizontal photospheric motions or not. Considering the magnetic field evolution, the main candidate is the differential rotation,

since shearing motions are evident only during the first rotation and inject a negligible amount of helicity compared to both the change in the corona and the helicity ejected in CMEs (see Section 3.2 and Table III). Previously Démoulin *et al.* (2002b) studied a classical bipolar active region (oriented east–west) where differential rotation injects magnetic helicity monotonically up to the maximum possible value. Here we select another kind of active region: AR 8100, in which the main polarities rotate one around the other. This implies that the magnetic helicity injected by differential rotation is no longer a monotonical function of time but that it has a maximum and even changes sign (due to the competition between twist and writhe helicity, Démoulin *et al.*, 2002a). This shows the effect of differential rotation on the helicity budget in a completely different case.

The evolution of AR 8100 can be separated into three periods. The first occurs in the period of a few days (2–5 November), when its coronal magnetic helicity was negative while differential rotation and shearing motions injected positive helicity of the same order of magnitude. A second period may be identified, corresponding to the last part of the first rotation, when its coronal helicity was changing from negative to positive so that no CME helicity budget can be derived with the present data. This is because to know the helicity sign, interplanetary observations of each CME-magnetic cloud would be required. Finally, during a third period, which includes rotations two to five, the AR coronal magnetic helicity was positive while differential rotation injected mainly negative helicity (see Figure 6).

Concerning the helicity budget in AR 8100, we have found that during the first period (2–5 November, 1997), the variation in the coronal helicity is two orders of magnitude larger than that injected by differential rotation and localized shearing motions, furthermore, of the wrong sign. Then, photospheric motions are actually depleting the coronal helicity instead of building it. At the same time the CMEs are likely to eject negative helicity, which is again two orders of magnitude larger than the one injected and of opposite sign.

From the second to the fifth rotation (the third period in the life of AR 8100), the coronal helicity is observed to decrease. During this period localized shearing motions were not evident in the AR. In the particular case of AR 8100, the intrinsic rotation of the region implies that at some time during the second rotation helicity injection by differential rotation becomes of negative sign (while maintaining the same velocity profile). This is due to the N–S orientation of the region and the dominance of writhe helicity. On one hand, the change of the sign of the helicity injected by differential rotation agrees with the coronal helicity decrease but, except for the last two rotations (starting at CMPs on 23 January and on 20 February), it stays one order of magnitude lower. Differential rotation is again destroying the coronal helicity, so one would expect from this an insignificant CME number. Instead, about one to two orders of magnitude more helicity was probably ejected via CMEs than is injected by differential rotation. Therefore, differential rotation cannot generate enough magnetic helicity to provide either the coronal helicity or

the helicity ejected into the interplanetary medium. This result agrees with that of Démoulin *et al.* (2002b).

Since differential rotation is not a good candidate to provide helicity to the coronal field, an alternative source is required. Even though during the first rotation strong shearing motions are observed in the main bipole and between it and the secondary emerging ones, from the second to the fifth rotation (which are the ones included in our helicity budget) there are no obvious horizontal photospheric motions which can provide the needed helicity. Thus, we conclude that the helicity comes from the last term on the right-hand side of Equation (5).

The budget of magnetic helicity may be written as

$$\Delta H_{\text{emergence}} = \Delta H_{\text{cor}} - \Delta H_{\text{d.r.}} + N H_{\text{CME}} , \tag{8}$$

where Δ means the variation of the helicity, N is the number of CMEs during the interval of time considered and H_{CME} is the mean helicity per CME. The fifth column of Table III gives the estimation of $\Delta H_{\text{cor}} - \Delta H_{\text{d.r.}}$. Then, the sum of this column with one of the last two columns (considering either observed or corrected CME numbers) in Table III will give an estimate for $\Delta H_{\text{emergence}}$ from the second to the fifth rotation (the first rotation is excluded because of the uncertainty in the sign of the helicity ejected by CMEs). It can be seen that there is a need for an injection of magnetic helicity during all rotations, even possibly during the second one if we consider the corrected CME number. This result is even more evident when we compare the total magnetic helicity budget from the second to the fifth rotation. From 68% to 96% of the helicity carried away by the CMEs should be provided by helicity transfer from the sub-photospheric layers (second term on the right hand side of Equation (5)). The magnetic helicity that was present in the corona at the beginning of the second rotation, but depleted by differential rotation, can account at most for 29% of the helicity in CMEs.

There is clear evidence of flux emergence during the third rotation (Section 2.2) which can account for the required helicity, and we infer from the change in sign of the coronal helicity that the flux emergence brings up positive helicity, as is expected for the southern hemisphere. However, we have no evidence of emergence during the last two rotations. This long-term input of magnetic helicity can be simply provided by the magnetic flux tube if it continues to move across the photosphere. This requires that it keeps some buoyancy. An alternative mechanism to this extended emergence, which does not require that the flux tube remains buoyant in the convective zone, has been considered by Longcope and Welsch (2000). They propose that for the steady state the coronal helicity is determined by the amount of twist present in the sub-photospheric part of the flux tube (this helicity transfer is provided by torsional Alfvén waves). Extending this model qualitatively to include CMEs, we can say that if the coronal helicity of the steady state is above the threshold of the global instability for the coronal field, a CME will occur, removing part of the helicity. Next, the imbalance of torque will again charge the coronal field with helicity typically in a day (see the time estimate of Longcope

and Welsch, 2000) and, the process will start again. In this approach, the coronal field is permanently, but in a time-dependent manner, filled by magnetic helicity from the convective zone until the flux tube twist is exhausted or the flux tube is destroyed by convective motions.

We conclude from the budget of magnetic helicity that the magnetic flux tube forming AR 8100 continues to emerge, or at least to provide an upward propagation of helicity to the corona, for a much longer time than the observed photospheric increase of magnetic flux.

Acknowledgements

L.M.G. is grateful to PPARC for postgraduate student funding. P.D., C.H.M. and M.C.L.F. acknowledge financial support from ECOS (France) and SETCIP (Argentina) through their cooperative science program (A01U04). L.v.D.G. is supported by the Hungarian Government grants OTKA T-032846, T-038013. P.D. and L.v.D.G. acknowledge the Hungarian–French S&T cooperative program. We are grateful to the Royal Society for the award of a European Joint Project grant. C.H.M. thanks the Solar Physics Group at MSSL for their hospitality and for an MSSL Visitor's Grant. These results were obtained in the framework of the projects OT/98/14 (K.U. Leuven), G.0344.98 (FWO-Vlaanderen), and 14815/00/NL/SFe(IC) (ESA Prodex 6). LVD is supported by Research Fellowship F/01/004 of the K.U. Leuven. The authors thank the MDI, EIT and LASCO consortia and the *Yohkoh*/SXT team for their data. SOHO is a project of international cooperation between ESA and NASA. *Yohkoh* is a mission of the Japanese Institute for Space and Astronautical Science. We acknowledge the SURF for providing data for this publication.

Appendix. Dependence of the Magnetic Helicity on the Magnetic Shear Coefficient α

The coronal field is computed under the linear force-free field assumption (Equation (1)). The vertical (or normal to the photosphere) component B_n of the field may be written:

$$B_n = \sum_{n_x=1}^{N_x} \sum_{n_y=1}^{N_y} \widetilde{B}_{n_x,n_y} \exp(-lz)\,, \tag{9}$$

where x, y are the Cartesian horizontal coordinates, z is the vertical coordinate, $\widetilde{B}_{n_x,n_y}$ is the Fourier amplitude of the harmonic (n_x, n_y), $l = \sqrt{k_x^2 + k_y^2 - \alpha^2}$, $k_x = 2\pi n_x/L$, $k_y = 2\pi n_y/L$, L being the horizontal extension of the computational box.

Following the results by Berger (1985), the relative magnetic helicity can be written as

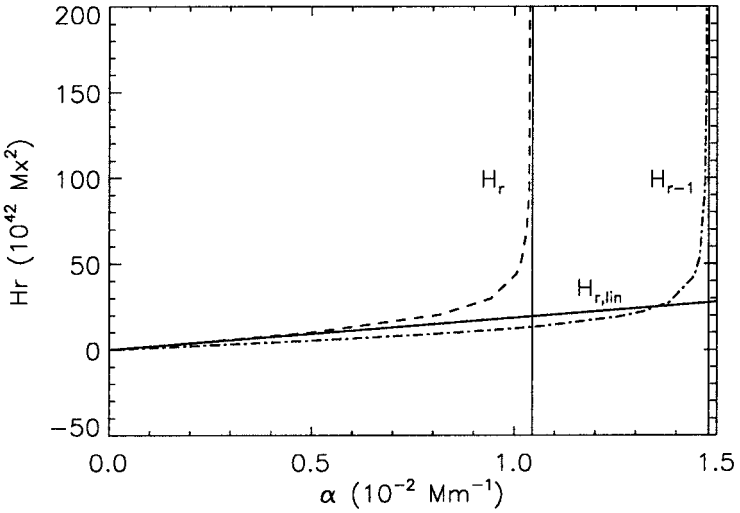

Figure 7. Dependence of the coronal magnetic helicity on the magnetic shear coefficient α.

$$H_r = 2\alpha \sum_{n_x=1}^{N_x} \sum_{n_y=1}^{N_y} \frac{|\widetilde{B}^2_{n_x,n_y}|}{l(k_x^2 + k_y^2)} \,. \tag{10}$$

As $l = \sqrt{k_x^2 + k_y^2 - \alpha^2}$ is in the denominator, this expression becomes infinite at each resonant value of α: $\alpha_r = \sqrt{k_x^2 + k_y^2}$. The lowest resonant value, $\alpha_{r,1}$ is for the harmonics $(n_x, n_y) = (1, 0)$ and $(0, 1)$. In practice the size of the box L is chosen to be large compared to the active region size then the amplitudes $\widetilde{B}_{n_x,n_y}$ of the harmonics with a low n_x and n_y are relatively small. Then it is only very close to the resonance that the magnetic helicity becomes large. This effect is illustrated in Figure 7 for the magnetic configuration on 27 December 1997 (curve labeled as H_r). If we subtract from H_r the contribution of the first diverging harmonics (1, 0) and (0, 1), we obtain the curve labeled as H_{r-1} that becomes divergent at the harmonic (1, 1).

A way to avoid the enhancement of the helicity close to the resonance values is to use a linearized version of Equation (10) versus α:

$$H_{r,\mathrm{lin}} = 2\alpha \sum_{n_x=1}^{N_x} \sum_{n_y=1}^{N_y} |\widetilde{B}^2_{n_x,n_y}|(k_x^2 + k_y^2)^{-3/2} \,. \tag{11}$$

This expression gives a lower bound of the magnetic helicity as deduced from a linear force-free field extrapolation (see Figure 7), which is the one we give in Table III for H_{cor}.

References

Alissandrakis, C. E.: 1981, *Astron. Astrophys.* **100**, 197.

Berger, M. A.: 1984, *Geophys. Astrophys. Fluid Dynamics* **30**, 79.

Berger, M. A.: 1985, *Astrophys. J. Suppl. Series* **59**, 433.

Berger, M. A.: 1988, *Astron. Astrophys.* **201**, 355.

Berger, M. A.: 2000, *Plasma Phys. Controlled Fusion* **41**, 167.

Berger, M. A. and Field, G. B.: 1984, *J. Fluid. Mech.* **147**, 133.

Bothmer, V. and Schwenn, R.: 1994, *Space Sci. Rev.* **70**, 215.

Brown, M. R., Canfield, R. C., and Pevtsov, A. A. (eds): 1999, *Magnetic Helicity in Space and Laboratory Plasmas, Geophy. Mon. Ser.* **111**, AGU, Washington.

Brueckner, G. E., Howard, R. A., Koomen, M. J., Korendyke, C. M., Michels, D. J., Moses, J. D. *et al.*: 1995, *Solar Phys.* **162**, 357.

Brueckner, G. E., Howard, R. A., Koomen, M. J., Korendyke, C. M., Michels, D. J., Moses, J. D. *et al.*: 1998, *J. Geophys. Res.* **103**, 277.

Canfield, R. C., Hudson, H. S., and McKenzie, D. E.: 1999, *Geophys. Res. Lett.* **26**, 627.

Chae, J.: 2001, *Astrophys. J.* **560**, L95.

Chae, J., Wang, H., Qiu, J., Goode, P. R., Strous, L., and Yun, H. S.: 2001, *Astrophys. J.* **560**, 476.

Cliver, E. W. and Hudson, H.: 2001, *J. Atmospheric Solar Terrest. Phys.*, in press.

Delaboudinière, J.-P., Artzner, G. E., Brunaud, J. *et al.*: 1995, *Solar Phys.* **162**, 291.

Delannée, C. and Aulanier, G.: 1999, *Solar Phys.* **190**, 107.

Démoulin P., Mandrini, C. H., van Driel-Gesztelyi, L., López Fuentes, M., and Aulanier, G.: 2002a, *Solar Phys.* **207**, 87.

Démoulin, P., Mandrini, C.H., van Driel-Gesztelyi, L. *et al.*: 2002b, *Astron. Astrophys.* **382**, 650.

DeVore, C. R.: 2000, *Astrophys. J.* **539**, 944.

Finn, J. H. and Antonsen, T. M.: 1985, *Comm. Plasma Phys. Contr. Fusion*, **9**, 111.

Green, L. M., Harra, L. K., Matthews, S. A., and Culhane, J. L.: 2001, *Solar Phys.* **200**, 189.

Hale, G. E. and Nicholson, S. B.: 1925, *Astrophys. J.* **62**, 270.

Hale, G. E., Ellerman F., Nicholson, S. B., and Joy, A. H.: 1919, *Astrophys. J.* **49**, 153.

Komm, R. W., Howard, R. F., and Harvey, J. W.: 1993, *Solar Phys.* **143**, 19.

Leamon, R. J., Canfield, R. C. and Pevtsov, A. A.: 2002, *J. Geophys. Res.*, in press.

Lepping, R. P., Burlaga, L. F., and Jones, J. A.: 1990, *J. Geophys. Res.* **95**, 11957.

Longcope, D. W. and Welsch, B. .: 2000, *Astrophys. J.* **545**, 1089.

López Fuentes, M., Démoulin, P., Mandrini, C. H., and van Driel-Gesztelyi, L.: 2000, *Astrophys. J.* **544**, 540.

López Fuentes, M. C., Mandrini, C. H., Démoulin, P., and van Driel-Gesztelyi, L.: 2001, in G. Mathys, S. K. Solanki, and D. T. Wickramasingle (eds.), *ASP Conf. Ser.: Magnetic Fields across the Hertzsprung-Rusell Diagram*, in press.

Low, B. C.: 1996, *Solar Phys.* **167**, 217.

Low, B. C.: 1997, in: N. Crooker, J. A. Joselyn, and J. Feynman (eds.), *Coronal Mass Ejections*, Geophysical Monograph 99, American Geophysical Press, Washington DC, p. 39.

Maia, D., Vourlidas, A., Pick, M., Howard, R., Schwenn, R., and Magalhes, A.: 1999, *J. Geophys. Res.* **104**, 12507.

Marubashi, K.: 1997, in: N. Crooker, J. A. Joselyn, and J. Feynman (eds.), *Coronal Mass Ejections*, Geophysical Monograph 99, American Geophysical Press, Washington DC, p. 147.

Pevtsov, A. A., Canfield, R. C., and Metcalf, T. R.: 1995, *Astrophys. J.* **440**, L109.

Richardson, I. G., Farrugia, C. J., and Burlaga, L. F.: 1991, *22nd. Int. Cosmic Ray Conf.* **15-93**, 9.

Richardson, I. G.: 1997, in: N. Crooker, J. A. Joselyn, and J. Feynman (eds.), *Coronal Mass Ejections*, Geophysical Monograph 99, American Geophysical Press, Washington DC, p. 189.

Rust, D. M.: 1994, *Geophys. Res. Lett.* **21**, 241.

Rust, D. M. and Kumar, A.: 1996, *Astrophys. J.* **464**, L199.

Scherrer, P. H., Bogart, R. S., Bush, R. I. *et al.*: 1995, *Solar Phys.* **162**, 129.
Seehafer, N.: 1990, *Solar Phys.* **125**, 219.
Shodhan, S., Crooker, N. U., Kahler, S. W., Fitzenreiter, R. J., Larson, D. E. *et al.*: 2000, *J. Geophys. Res.* **105**, 27261.
Sterling, A. C. and Hudson, H. S.: 1997, *Astrophys. J.* **491**, L55.
Thompson, B. J., Gurman, J. B., Neupert, W. M. *et al.*: 1999, *Astrophys. J.* **517**, L151.
Tsuneta, S. *et al.*: 1991, *Solar Phys.* **136**, 37.
van Driel-Gesztelyi, L., Schmieder, B., and Poedts, S.: 2001, *Proc. SOLSPA-2001 Euroconference*, ESA SP-477, in press.
Webb, D. F., Cliver, E. W., Crooker, N. U., St. Cry, O. C., and Thompson, B. J.: 2000, *J. Geophys. Res.* **105**, 7491.
Yan, Y., Yang, L., Maki, A., and Fengsi, W.: 2001, *Solar Phys.* **201**, 337.
Yurchyshyn, V. B., Wang, H., Goode, P. R., and Deng, Y.: 2001, *Astrophys. J.* **563**, 381.
Zarro, D., Sterling, A., Thompson, B., Hudson, H., and Nitta, N.: 1999, *Astrophys. J.* **520**, 139.
Zhao, X. P., Hoeksema, J. T., and Marubashi, K.: 2001, *J. Geophys. Res.* **106**, 15643.
Zirin, H.: 1988, *Astrophysics of the Sun*, Cambridge University Press, Cambridge, p. 308.